Invited Review Paper

Recent Advances in X-ray Phase Imaging

Atsushi MOMOSE[*]

Department of Advanced Materials Science, Graduate School of Frontier Sciences, The University of Tokyo,
5-1-5 Kashiwanoha, Kashiwa, Chiba 277-8561, Japan

Since the middle of the 1990s, X-ray phase imaging including phase tomography has been attracting increasing attention. The advantage of X-ray phase imaging is that an extremely high sensitivity is achieved for weak-absorbing materials, such as biological soft tissues, which generate a poor contrast by conventional methods. Medical and biological imaging is the main target of X-ray phase imaging, and several trials using synchrotron radiation sources and laboratory sources have been made. Measuring and controlling the X-ray phase are also significant for X-ray microscopy with a high spatial resolution, and innovative techniques are attracting intense interest. The progress of X-ray phase imaging is supported by the developments in X-ray sources such as third-generation synchrotron radiation sources, optical elements, and image detectors. This article describes the advantages of using X-ray phase information and reviews various techniques studied for X-ray phase imaging. [DOI: 10.1143/JJAP.44.6355]

KEYWORDS: X-rays, tomography, X-ray microscopy, synchrotron radiation, interference, interferometer, coherency, phase contrast, phase retrieval

1. Introduction

The penetrating power of X-rays has been used to reveal hidden inner structures nondestructively since the discovery of X-rays by Röntgen in 1895. X-ray imaging is nowadays indispensable in a variety of fields, including medicine and industry. However, since an X-ray contrast is generated by the difference in attenuation, weak-absorbing materials are not imaged satisfactorily in principle, limiting the range of application for X-ray imaging. The X-ray absorption coefficient is roughly proportional to the fourth power of the atomic number Z, apart from the jumps at absorption edges.[1] Therefore, materials consisting of low-Z elements produce poor contrast. Soft tissues in a body and organic materials are difficult to image with X-rays. In order to overcome this difficulty, contrast media or staining is occasionally used. However, such treatments are not always possible and there is the possibility that the treatments will cause structural changes.

In this decade, making the use of X-ray phase information for imaging has attracted attention.[2] As described below, since the interaction cross section of X-ray phase shift is much larger than that of absorption, an extremely high sensitivity is attained by phase-contrast X-ray imaging.[3] Therefore, the medical application of this method is attractive because soft tissues can be imaged without contrast media and/or a serious dose. Its application to X-ray microscopy is also attractive because even tiny structures produce a phase contrast clearer than an absorption contrast, leading to higher spatial resolution.

In this article, *phase imaging* is used to describe not only phase-contrast methods, which simply record contrasts generated by the participation of the X-ray phase shift, but also the methods that determine the phase shift quantitatively. The research activity of the latter in particular is growing markedly, enabling sophisticated applications; *X-ray phase tomography*[4] is a prominent achievement by quantitative phase-shift measurement.

X-ray computed tomography (X-ray CT) is well developed as a three-dimensional imaging method. Sectional images on planes parallel to the X-ray propagation direction can be reconstructed from images obtained in the plural projection directions. Its image contrast depends on X-ray absorption, and therefore the problem of poor sensitivity to weak-absorbing structures still exists. X-ray phase tomography was attained by introducing the technique of X-ray phase imaging into X-ray CT. In this case, because the X-ray phase shift is expressed as a projection of the refractive index, a reconstructed three-dimensional image corresponds to a map of the refractive index. X-ray phase tomography of course inherits its high sensitivity from X-ray phase imaging, enabling three-dimensional imaging of soft tissues.

Since phase information is lost in measuring X-ray transmission images, several techniques have been contrived in X-ray optics to convert the X-ray phase shift to X-ray intensity modulation. Because of the short wavelength of X-rays, comparatively low coherence of X-rays, and limited choices of X-ray optical elements, the construction of phase-sensitive optics is not as flexible as in the visible-light region.

Nevertheless, recent developments in X-ray sources and X-ray optical elements have opened a door to phase imaging. In this article, the advantages of using X-ray phase information are described first, and recent X-ray phase imaging studies including X-ray phase tomography are reviewed. Finally the prospects of this field are presented.

2. Advantages of X-ray Phase Imaging

2.1 Sensitivity

Optical density $D(x, y)$, which is the logarithm of X-ray transmittance $T(x, y)$, and phase shift $\Phi(x, y)$ are expressed as

$$D(x, y) = -\ln T(x, y) = \int \mu(x, y, z)\, dz, \tag{1}$$

$$\Phi(x, y) = \frac{2\pi}{\lambda} \int \delta(x, y, z)\, dz, \tag{2}$$

where λ is the X-ray wavelength, and $\mu(x, y, z)$ and $\delta(x, y, z)$ are the linear absorption coefficient and refractive index decrement from unity of the material through which the X-rays penetrate, respectively. Here, X-rays are assumed to go straight through the material along the z-axis.

[*]E-mail address: momose@exp.t.u-tokyo.ac.jp

From an atomic point of view, $\mu(x, y, z)$ and $\delta(x, y, z)$ are written as

$$\mu(x, y, z) = \sum_k N_k(x, y, z)\mu_k^a, \tag{3}$$

$$\delta(x, y, z) = \frac{r_e\lambda^2}{2\pi} \sum_k N_k(x, y, z)(Z_k + f_k'), \tag{4}$$

where $N_k(x, y, z)$, μ_k^a, Z_k, and f_k' are the atomic density, atomic absorption coefficient (or absorption cross section), atomic number (that is, number of electrons per atom), and the real part of the anomalous dispersion correction of element k, respectively. r_e is the classical electron radius. It should be noted that μ_k^a involves the effects of photoelectron absorption and the loss due to both of Thomson and Compton scatterings. The substitutions of eq. (3) into eq. (1) and eq. (4) into eq. (2) yield

$$D(x, y) = \int \sum_k N_k(x, y, z)\mu_k^a \, dz, \tag{5}$$

$$\Phi(x, y) = \int \sum_k N_k(x, y, z)p_k \, dz, \tag{6}$$

where

$$p_k \equiv r_e\lambda(Z_k + f_k') \tag{7}$$

corresponds to the cross section of the X-ray phase shift. Thus, the difference between $D(x, y)$ and $\Phi(x, y)$ is attributed to the difference between μ_k^a and p_k. In order to show the sensitivity achievable by relying on the absorption and phase shift, μ_k^a and p_k are plotted versus the atomic number in Fig. 1 for various X-ray energies. p_k is always larger than μ_k^a, and the ratio p_k/μ_k^a is almost 10^3 for low-Z elements. Thus, if phase information is effectively used for imaging, the sensitivity to soft structures is improved by about a thousand times.[3]

From a macroscopic point of view, the complex refractive index ($n = 1 - \delta + i\beta$) would be comprehensive in comparison. The linear absorption coefficient μ is related to the imaginary part of n with

$$\beta = \frac{\lambda}{4\pi}\mu. \tag{8}$$

Values of δ and β of representative materials for 20 keV X-rays are shown in Table I. Consistently with Fig. 1, δ/β is about 10^3 for materials consisting of low-Z elements.

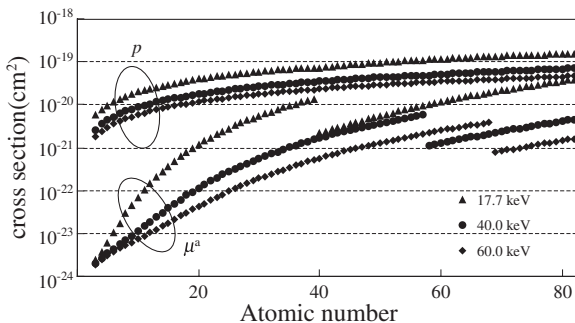The energy dependences of μ_k^a and p_k are presented for

Fig. 1.   Interaction cross sections of absorption (μ^a) and phase shift (p) vs the atomic number.

Table I.   Complex refractive indices given by $1 - \delta + i\beta$ and δ/β of representative materials at 20 keV.

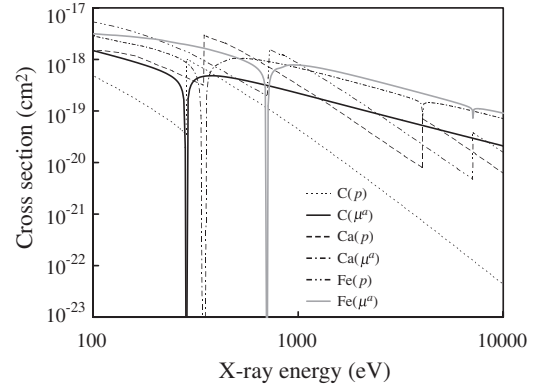| Materials	δ	β	δ/β
Polystyrene	5.0×10^{-7}	3.2×10^{-10}	1.6×10^3
Water	5.8×10^{-7}	6.0×10^{-10}	9.7×10^2
Glass	1.3×10^{-6}	2.9×10^{-9}	4.5×10^2
Silicon	1.2×10^{-6}	4.9×10^{-9}	2.4×10^2
Iron	3.8×10^{-6}	9.7×10^{-8}	3.9×10^1

Fig. 2.   Interaction cross sections of absorption (μ^a) and phase shift (p) of carbon, calcium and iron atoms vs X-ray energy.

carbon, calcium, and iron atoms in Fig. 2. Apart from absorption-edge structures, both μ_k^a and p_k increase with the decrease in X-ray energy. It should be noted that the ratio p_k/μ_k^a in the soft X-ray region is not as large as in the hard X-ray region. Thus, the advantage of phase contrast is more prominent in the hard X-ray energy region.

2.2   Required energy bandwidth

The comparison described above is given for monochromatic X-rays. Conventionally, particularly in laboratories, X-rays of a broad energy spectrum are used for imaging. As discussed below, even in phase-contrast X-ray imaging, the X-ray bandwidth can be broadened to a certain extent.

From eqs. (2) and (4), the phase change $\Delta\Phi$ caused by the spectral change $\Delta\lambda$ is given by

$$\Delta\Phi \approx r_e\Delta\lambda \int \sum_k N_k(x, y, z)(Z_k + f_k') \, dz,$$

$$\approx r_e\Delta\lambda \int \rho(x, y, z) \, dz, \tag{9}$$

where $\rho(x, y, z)$ is the electron density, which is a good approximation for materials consisting of low-Z elements because absorption edges do not exist in the hard X-ray energy region and $f_k' \ll Z_k$. Assuming a criterion like the Rayleigh's quarter wavelength rule for interference (i.e., $\Delta\Phi < \pi/2$), one finds that $\Delta\lambda$ is independent of λ and satisfies

$$\Delta\lambda \lesssim \frac{\pi}{2r_e t\rho} \tag{10}$$

for an object of a thickness t and a uniform ρ. In the case of water, $\rho = 3.5 \times 10^{29}$ m^{-3}, and then $\Delta\lambda t \lesssim 1.6 \times 10^{-15}$ m^2. This implies for instance that the contrast of a 100 μm bubble in water does not smear out in phase imaging in
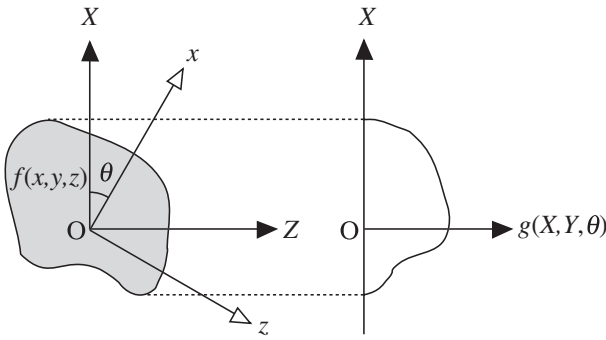
Fig. 3. Geometry of computed tomography. In the case of phase tomography, $f(x, y, z)$ and $g(X, Y, \theta)$ corresponds to the phase shift Φ and refractive index decrement δ, respectively.

principle even if $\Delta\lambda$ is 0.01 nm. Thus, phase-contrast X-ray imaging does not require strict monochromaticity for contrast generation, provided that the optical elements allow the bandwidth.

2.3 Phase tomography

Computed tomography enables the reconstruction of a scalar field $f(x, y, z)$ when its projection data $g(X, Y, \theta)$ shown in Fig. 3 are measured in plural directions. In conventional X-ray CT, $f(x, y, z)$ and $g(X, Y, \theta)$ correspond to μ and D, respectively, which are related by eq. (1). According to eq. (2), where the phase shift Φ is given by a projection form of δ, if Φ is measured quantitatively, one can reconstruct δ, which is called *phase tomography*. The high sensitivity attained by using X-ray phase information is of course inherited.

3. Requirements for X-ray Phase Imaging

3.1 Coherency

In order to generate a contrast with phase information, one needs to use a wave that has a defined phase. In other words, a coherent X-ray beam, the coherence degree of which does not need to be complete, should be used. The coherency can be evaluated along the optical axis and perpendicularly to it separately, that is, temporal (longitudinal) coherency and spatial (transverse) coherency. The temporal coherence length ℓ_t is related to the Fourier transform of the spectrum and is roughly given by $\ell_t \sim \lambda^2/\Delta\lambda$, and therefore enlarged by monochromatizing. In the hard X-ray region (typically $\lambda \approx 0.1$ nm), a double-crystal silicon monochromator is normally used at synchrotron radiation beamlines, and a typical bandwidth is $\Delta\lambda/\lambda \approx 10^{-4}$, giving $\ell_t \approx 1\,\mu$m. By forming more sophisticated crystal arrangements, it is easy to attain $\Delta\lambda/\lambda \approx 10^{-5}$ and $\ell_t \approx 10\,\mu$m. In the soft X-ray region ($\lambda \approx 1$–10 nm), a grating monochromator is employed whose bandwidth is 10^{-2}–10^{-4}, giving $\ell_t \approx 0.1$–$100\,\mu$m.[5] In many imaging applications, the temporal coherence length is satisfactory.

The spatial coherency influences imaging quality more sensitively. The degree of spatial coherence is given by the Fourier transform of the intensity distribution of an X-ray source (the van Cittert–Zernike theorem).[6] The spatial coherence length ℓ_s is given by $\ell_s \sim \lambda/(2\pi\Delta\theta)$, where $\Delta\theta$ is the angular size of an X-ray source. Therefore, the smaller the source, the higher the spatial coherence. In order to

ensure that the spatial coherence length is sufficient for phase imaging, coherence filters, such as a narrow aperture and a crystal collimator, are adopted, submitting to the decrease in X-ray intensity. Third-generation synchrotron facilities provide X-rays from electron bunches whose size is a few tens of microns vertically and a few hundreds of microns horizontally. Because X-rays are available about 100 m downstream from the source (electron bunches), the spatial coherence length ℓ_s is roughly $100\,\mu$m vertically and $10\,\mu$m horizontally, which is sufficiently high for most phase imaging methods.

3.2 Optical elements

One method of detecting $\Phi(x, y)$ is by using interference. An interference pattern generated with a coherent plane wave is given by

$$I(x, y) = |1 + \exp[i\Phi(x, y)]|^2$$
$$= 2[1 + \cos\Phi(x, y)]. \quad (11)$$

Interference fringes are thus contours of a constant phase shift appearing every 2π. Another method of detecting the influence of the phase shift is to measure the refraction of X-rays. Waves propagate in the direction perpendicular to the wavefront in vacuum, and the beam deflection angle (α_x, α_y) is related to $\Phi(x, y)$ with

$$(\alpha_x, \alpha_y) = \frac{\lambda}{2\pi}\nabla\Phi(x, y). \quad (12)$$

Thus, the differential phase information is obtained in this case. Most of the methods for phase-sensitive X-ray imaging make use of either or both of the effects of eqs. (11) and (12). Here, optical elements used in phase-sensitive X-ray optics are outlined.

A focusing device[7] is indispensable to the construction of a microscope, but no X-ray transmission lenses are available, except for a compound X-ray refractive lens that was reported recently,[8] because the refractive indices of all materials are close to unity, as mentioned above. Focusing mirrors and Fresnel zone plates are mainly used for X-ray microscopy.[9] The quality requirements of the surface finish and slope error of the mirrors are strict because of the short X-ray wavelength. The thickness of the outermost zone of the Fresnel zone plate should be as narrow as possible because the focusing quality is determined by it.

When such focusing devices function ideally, it implies that the X-ray phase is being controlled properly. Then, the construction of phase-sensitive X-ray microscopes becomes feasible as well. As introduced in §4.1, Fresnel zone plates in particular play an important role in recent developments of phase-sensitive X-ray microscopes.

For interferometric methods, at least two coherent beams must be generated by dividing a single beam. Both wavefront division and amplitude division are used in the X-ray region. Wavefront division is comparatively easy, and Young's double slits, Fresnel bimirrors, and prisms are applicable if the spatial coherency is sufficient. Amplitude division is superior in that the spatial coherency is not as essential as it is in the case of wavefront division. In the hard X-ray region, a perfect crystal is available for amplitude division, and crystal interferometers are used for phase imaging, as introduced in §4.2.1. Recently, transmission

gratings have also been available for constructing X-ray interferometers, as described in §4.2.2. In the soft X-ray region, since crystals do not function, reflection gratings and self-standing multilayers are used, as described in §4.2.4.

In order to generate a contrast relying on hard X-ray refraction, crystals are used as introduced in §4.3. The crystal device functions not only as a narrow band-pass filter but also as a collimator.[10] The angular acceptance of the Bragg diffraction by a perfect crystal is of the order of 1–10 µrad, enabling the selection of refracted X-rays.

If a highly coherent beam is available, Fresnel or Fraunhofer diffraction of X-rays can be observed when a wavefront is deformed by a sample and the distance between the sample and image detection plane is of the order of one meter. The diffraction pattern is used for phase-sensitive imaging, as described in §4.4.

One should pay attention to the speckle pattern generated by a coherent beam due to the inhomogeneity or imperfection of optical elements and/or Be windows, which are commonly used in beamlines to separate an X-ray source in vacuum and atmosphere. Of course, the speckle pattern that disturbs imaging in this case can be removed by improving the quality of the optical elements and windows. Otherwise, a diffuser can be used, which reduces spatial coherency moderately.[11]

3.3 Image detector

As for X-ray image detectors,[7] no special contrivance is needed for phase imaging provided that the spatial resolution is sufficient to resolve interference fringes. It should rather be emphasized that digital image processing is important for X-ray phase imaging. Taking a picture of a phase-contrast image is the simplest approach. Of course it is useful in some cases, but occasionally it is hard to extract structural information directly from the picture. Interferograms or holograms are complicated and their image processing, which extracts phase information, is necessary. For three-dimensional observation under the tomographic configuration, digital image processing is also indispensable. The progress of X-ray phase imaging would be slower without digital image processing.

Exposure time for obtaining an image depends on the pixel size of the detector. It should be noted that downsizing a pixel by a factor of two to improve the spatial resolution, particularly of radiographs, requires an increase in the exposure by more than four times. The smaller the pixel is, the thinner the X-ray-sensitive region of the detector should be in order to avoid blurring. Because all X-ray detectors sense an X-ray by absorption, the thin sensor causes a decrease in efficiency and accordingly an increase in exposure. Bright X-rays are therefore preferable, and it should be emphasized that the increase in the requirements to detectors and sources can be moderated by making use of phase contrast. Standard exposure time for recording a typical phase-contrast image is roughly 0.1–10 s using monochromatic synchrotron hard X-rays with a pixel size of a few microns.

4. Phase-Sensitive Methods

4.1 Microscopic technique

Since the wavelength of X-rays is a thousand times shorter than that of visible light, extremely high resolution is expected with X-ray microscopy. Soon after the discovery of X-rays in 1895, seeing tiny structures in radiographs was attempted and the history of X-ray microscopy began.[9] Although the field of X-ray microscopy was not usefully developed for some time after this because the performance of X-ray optical elements was poor, recent developments in the fabrication techniques of X-ray optical elements have been notable.

Spatial coherency is another important factor in X-ray microscopy. Under illumination of poor spatial coherency, the performance of optical elements cannot be exhibited fully, degrading imaging quality. A simple way to obtain a coherent beam is to use a pinhole. However, the loss of X-rays is crucial, and therefore a bright X-ray source is needed. Synchrotron radiation sources (particularly undulators that emit brilliant X-rays by undulating the trajectory of electron bunches) met this demand, and the field of X-ray microscopy thus had the opportunity to develop.

The progress in X-ray optics and X-ray sources has also been stimulating the development of phase-sensitive X-ray microscopy. Here, some techniques that use X-ray phase information are described for microscopic imaging.

4.1.1 Zernike's X-ray microscopy

Phase contrast was introduced into visible-light microscopy by Zernike[12] about seventy years ago. X-ray phase contrast[13] was reported in 1994 after the development of high-quality Fresnel zone plates in the soft X-ray energy region. A soft X-ray phase-contrast microscope was constructed for use in the water window, which is the spectral region between the K absorption edges of carbon and oxygen, where at that time most X-ray microscopy study was done because the absorption contrast between protein and water was prominent. Although the advantage of using phase information was successfully demonstrated in the water window, the research activity of phase-contrast X-ray microscopy is shifting toward the hard X-ray region[11,14,15] since the merit of phase contrast is more conspicuous for harder X-rays, as suggested in Fig. 2.

4.1.2 X-ray holography

Holography is straightforward as a technique using the wave nature of light.[16] X-ray in-line holography was attempted earlier than Zernike's phase-contrast X-ray microscopy. The first successful experiment of soft X-ray holography was reported about thirty years ago.[17,18] Fourier-transform X-ray holography is superior to in-line X-ray holography in the spatial resolution, and demonstrations were reported using Fresnel zone plate optics[19] and lensless optics.[20] In the hard X-ray region, Fourier-transform holography was also reported using a Fresnel zone plate[21,22] and a prism.[23]

In the visible-light region, holography is known as a three-dimensional imaging technique. Therefore, one may expect three-dimensional images by X-ray holography. However, the depth resolution of an image reconstructed from an X-ray hologram is much worse than the transverse resolution because nearly all X-rays are forward-scattered and the signal of a large momentum transfer is faint. Therefore, it is difficult to reconstruct a three-dimensional image from a

single X-ray hologram. Even if a holographic scheme is introduced into the imaging principle, multiple holograms are needed to produce a three-dimensional image, as is the case with X-ray CT.

4.1.3   Differential X-ray microscopy

The generation of differential phase contrast in X-ray microscopy has also been studied. Wilhein *et al.* developed a twin zone plate[24] which consisted of two similar zone-plate patterns on the both sides of a Si_3N_4 membrane. The centers of the patterns were slightly displaced from each other, and therefore, when the twin zone plate was used as an objective, two images were formed coherently with a small shear resulting in a differential phase contrast.

Differential phase contrast was generated also in scanning X-ray microscopy. While an image is formed conventionally by measuring the transmittance at every raster-scan point, the deflection of X-ray beams caused by the refraction at a sample was measured with a charge-coupled device (CCD)[25,26] and a wedge absorber detector.[27]

4.1.4   Coherent diffraction microscopy

X-ray crystallography is well established as a method of resolving the average structure of the unit cell of a crystal from Bragg spots. The technique has been expanded into nonperiodic materials. In this case, the intensity of the diffraction field is sampled. Although the diffraction field is extremely weak, the development of third-generation synchrotron radiation has enabled such measurements. Of course, there is the well-known 'phase problem', in which the phase information of the diffraction field is needed to determine the structure of a sample. The phase problem is solved by means of iterative calculation from an over-sampled image.[28] Here, a sample is required to be surrounded by a 'support', where the electron density is assumed to be zero.

A complex image obtained by combining the amplitude obtained from a measured diffraction pattern with an initial random phase is here denoted by F_0. The inverse Fourier transform of F_0, which is denoted by ρ_0, should be the electron density if the assumed phase is correct. Because in this first iteration the phase was random, the value of ρ_0 in the 'support' region is of course nonzero. Therefore, a procedure is followed to drive the value closer to zero. Furthermore, when the real part of ρ_0 inside the 'support' frame is negative, another procedure is followed to drive it close to zero. Next, the modified ρ_0 is converted to the reciprocal space by Fourier transform resulting in $\tilde{F}_0$. Then, $|\tilde{F}_0|$ is replaced with the experimental data, maintaining the phase as it is, and thus F_1 is obtained for the next iteration.

The spatial resolution attained with this technique is preeminent, as demonstrated by Miao *et al.*[29] They observed Ni patterns formed on both sides of a Si_3N_4 membrane 1 μm thick with 6.2 keV undulator X-rays resulting in a spatial resolution of 8 nm two-dimensionally [Fig. 4(a)]. As in the case of X-ray holography, it is difficult to determine the electron density three-dimensionally from a single diffraction pattern. Therefore, multiple diffraction patterns were recorded by tilting the sample, and a three-dimensional image with a 50 nm spatial resolution was attained as shown in Fig. 4(b). The Ni patterns fabricated on both sides of the
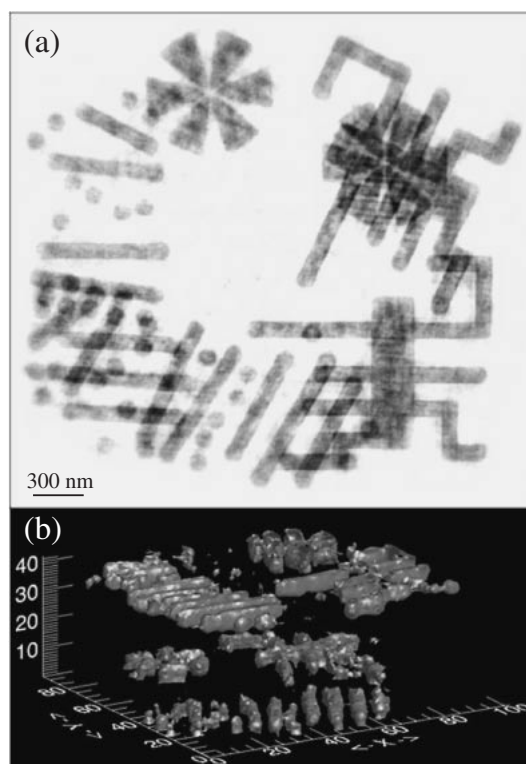

Fig. 4.   Two-dimensional image (a) and three-dimensional image (b) of Ni patterns formed on both sides of a Si_3N_4 membrane reconstructed from oversampled diffraction patterns.[29] The finest division of the Z-axis is 25 nm.

membrane were thus revealed separately. By using future brilliant X-ray sources, a molecular resolution is in principle expected.

4.2   Interferometric technique

Interferometry would be the most comprehensive way of detecting the phase shift. It is clear that various techniques of phase imaging developed in the visible-light region and others are available when an X-ray interferometer is constructed. However, because of the short wavelength of X-rays, the construction of X-ray interferometers is not straightforward. In order to form X-ray beam paths generating a stable interference, optical elements of an X-ray interferometer should be sufficiently stable so that the deviation of the optical path length is smaller than the wavelength. Although it is a challenging task, various X-ray interferometers have been developed and used for X-ray phase imaging.

One approach to the realization of X-ray interferometers is to use paraxial rays. Since the displacement of optical elements is less influential to the phase of X-rays that are less deflected from the primary beam axis, such X-ray interferometers are comparatively insensitive to vibration.

Another approach is to use crystal optics, which is characteristic of hard X-ray interferometry. The stability of an interferometer is ensured by cutting its entire body monolithically out of a single-crystal ingot.

Furthermore, the recent development of X-ray sources such as undulators and laser plasma sources is making it possible to acquire an image with a short exposure by virtue of their high brilliance. The influence of vibration is avoided

by taking a stop-motion picture if the instability time constant of the interferometer is longer than the exposure time. Although its application to phase imaging is limited, a variety of X-ray interferometers can be constructed and used.

Although X-ray interferometric imaging has already been reviewed by the author,[30,31] the activities are introduced again with recent results and another viewpoint below.

4.2.1 Crystal interferometer

One may imagine that X-ray interferometry was developed in the soft X-ray region first and then in the hard X-ray region according to the wavelength. However, a crystal hard X-ray interferometer was successfully operated earlier. This is because hard X-rays can be used in atmosphere while soft X-rays should be used in vacuum, and also because crystals, which have the most ideal periodic structures, are available for use with hard X-rays, while the wavelengths of soft X-rays do not match the periods of crystals and instead artificial optical elements must be developed. Here, X-ray phase imaging using hard X-ray interferometers fabricated from a perfect silicon crystal is described.

Figure 5(a) shows the first crystal X-ray interferometer reported by Bonse and Hart in 1965.[32] The entire body of the interferometer was monolithically cut out from a silicon crystal. Three parallel lamellae are formed with a constant spacing. The lamellae function as beam splitters when an X-ray is incident at the Bragg diffraction condition on a lattice plane perpendicular to the surface of the lamellae.

The amplitude of an X-ray is coherently divided into diffracted and forward-diffracted beams outgoing from the opposite side of the lamella. X-rays thus divided by the first lamella are divided again by the second lamella in the same manner. Two beams overlapping at the third lamella are also divided and interference is observed in the beams outgoing from the third lamella. Because of its monolithic configuration, no mechanical tuning is needed except in the arrangement of the interferometer so that the Bragg diffraction condition is satisfied. It should be noted that the lamellae have a function of coherence filtering through Bragg diffraction. Furthermore, the optical system corresponds to the Mach-Zehnder interferometer, which causes interference between two arms with an almost zero optical

path difference. Therefore, if the spacings between the lamellae are the same within an error of a few tens of microns, interference can be detected even using a normal laboratory source.

In an early stage, a picture of an interference pattern was taken for a sample sliced to prevent constant-thickness fringes from appearing.[33] Later, techniques of subfringe analysis were introduced with a digital image detector to determine the phase shift.[3,4] A sample thereby no longer needed to be sliced, and the first X-ray phase tomography, described below, was attained.[4] The high sensitivity of this method was demonstrated with various biological imaging results.[34–38] Some details of the method are introduced below.

The phase shift caused by an object placed in one arm generates an interference pattern, which is in general given by

$$I(x, y) = a(x, y) + b(x, y)\cos[\Phi(x, y) + \Delta(x, y)], \quad (13)$$

where $a(x, y)$ and $b(x, y)$ are the average intensity and fringe contrast, respectively. The interferometer has some residual strain that normally generates a built-in fringe pattern, and the influence is involved in $\Delta(x, y)$.

Often $\Delta(x, y)$ is not negligible and $\Phi(x, y)$ exceeds 2π, making the interference pattern too complicated for grasping structural information by eye. Even in such a situation, $\Phi(x, y)$ is determined using subfringe analyses. One approach is the Fourier-transform method;[39] by introducing fine carrier fringes, for instance with a wedge phase shifter, $\Phi(x, y)$ can be obtained by Fourier filtering. Another approach is the fringe-scanning method,[40] by which the spatial resolution is not affected while the spatial resolution attained with the Fourier-transform method is limited by the spacing of the carrier fringes.

Phase tomography is mainly performed with the fringe-scanning method because of the advantage of the spatial resolution. The fringe-scanning method processes multiple interference patterns observed by varying the phase difference between the two arms, for instance by using a tunable phase shifter. When interference patterns

$$
\begin{aligned}
I_k(x, y) = a(x, y) \\
+ b(x, y)\cos[\Phi(x, y) + \Delta(x, y) + 2\pi k/M] \quad (14) \\
(k = 1, 2, \ldots, M)
\end{aligned}
$$

are obtained ($M \geq 3$), $\Phi(x, y)$ is determined from

$$\Phi(x, y) + \Delta(x, y) = \arg\left[\sum_{k=1}^{M} I_k(x, y)\exp\left(-2\pi i\frac{k}{M}\right)\right]. \quad (15)$$

$\Delta(x, y)$ can be determined separately without a sample [$\Phi(x, y) = 0$]. For phase tomography, this measurement is repeated while rotating the sample.

Figure 6 is a three-dimensional image of tissue of a rat kidney reconstructed by phase tomography.[31] Tubules in the tissue, a part of which were clogged by protein, were revealed without using contrast media. Glomeruli were also depicted clearly. The image mapping δ corresponds approximately to a density map, and the detection limit of density deviation was evaluated to be $1.2\,\text{mg/cm}^3$.

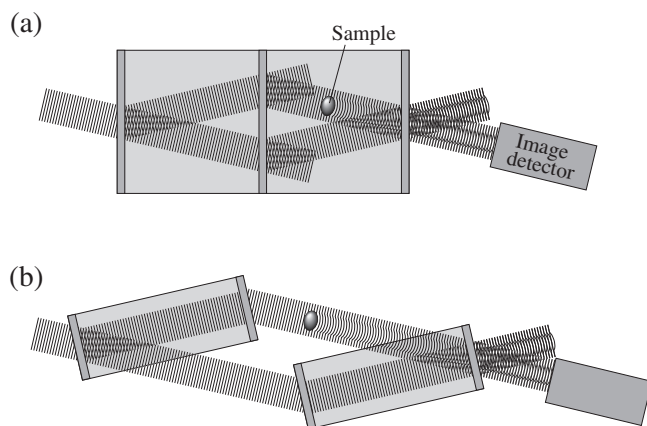Because of the argument operation in eq. (15) whose

Fig. 5. Crystal X-ray interferometers of a monolithic type (a) and a non-monolithic type (b), which was developed to expand its field of view.
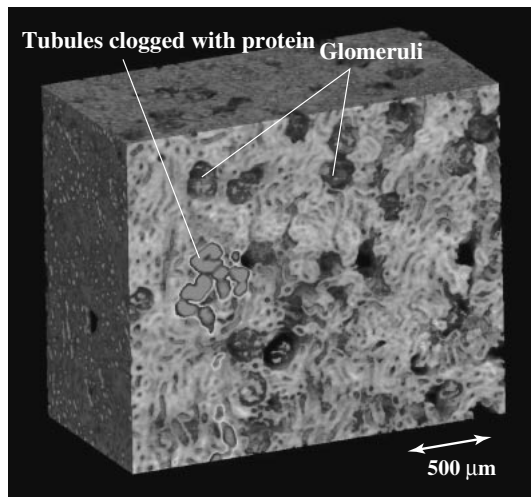
Fig. 6.   Image of a tissue of a rat kidney measured by phase tomography with 12.4 keV undulator X-rays using a crystal X-ray interferometer.[31]
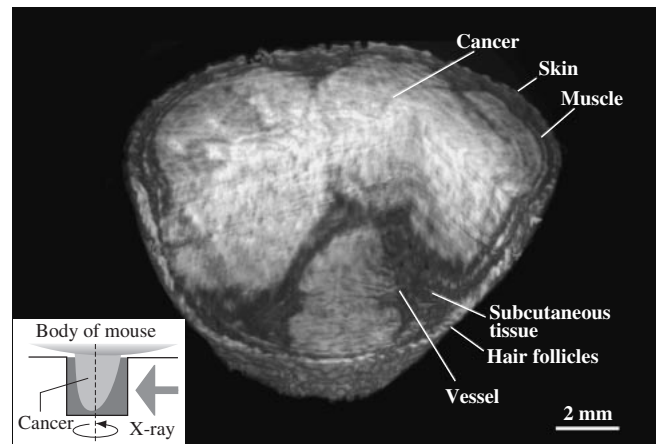

Fig. 7.   *In vivo* image of colon cancer implanted in a nude mouse observed by phase tomography using a two-crystal X-ray interferometer with 35 keV X-rays.[43] The inset describes the setup for the measurement of a protruding cancer tissue.

value ranges from $-\pi$ to π, jumps of 2π are inevitably contained in a resultant image when $\Phi(x, y)$ exceeds 2π. Therefore a process called *phase unwrapping* is needed to remove the jump by adding or subtracting 2π to or from one side of the jump. This procedure is successful when the signal-to-noise ratio of the image is sufficiently high and phase variation is not too abrupt. However, errors occur because the jumps occasionally become unclear. To overcome this difficulty, sophisticated phase unwrapping algorithms are developed, and a cut-line algorithm[41] was used for the phase tomography described above.

The spatial resolution is limited by the blurring effect at the lamella downstream of the sample even when a high-resolution image detector is used. The effect is caused by the dynamical diffraction; the path of an X-ray inside the crystal lamella is extremely sensitive to its incident angle. The angular deviation of an incident X-ray, which always occurs due to the refraction at the sample, is amplified about ten thousand times inside a crystal. In order to suppress this effect, an X-ray interferometer with a thin lamella 40 μm thick was fabricated,[38] with which Fig. 6 was measured.

The field of view produced with the monolithic X-ray interferometer is limited by the diameter of the FZ-silicon ingot from which the interferometer is cut out. In order to overcome this limit, a configuration consisting of two independent crystal blocks, shown in Fig. 5(b), was developed. Although the advantages of the monolithic structure were given up, a field of view of $60 \times 30\,\text{mm}^2$ was successfully generated at 17.7 keV and used for phase imaging.[42] The influence of vibration was reduced by increasing the rigidity of the alignment stage, and a feedback control was adopted for the stage so that the drift of interference fringes was canceled. Figure 7 shows a result of *in vivo* phase tomography performed with this system. In order to shorten the scan time, the Fourier-transform method was used, with which Φ can be obtained from a single interferogram, compromising a certain degradation of the spatial resolution. A three-dimensional image of colon cancer implanted in a nude mouse was successfully obtained with 35 keV X-rays.[43]

In addition to the configuration of the interferometer described above, other varieties of crystal interferometers have also been studied. A shearing interferometer[44] was fabricated by monolithically forming two pairs of lamellae with a narrow gap. An interferometer with a so-called Bragg-case beam splitter was also operated for phase imaging, with the aim of a better spatial resolution;[45] while X-rays go through the lamella in the interferometers described above, a beam is partially reflected on the lamella surface of this interferometer. Then, the X-rays that passed through a sample can be recombined with a reference beam without going through a lamella, thus avoiding the image blurring effect described above.

4.2.2   Grating interferometer

Grating interferometers have been operated as well in the hard X-ray region using two phase gratings and a crystal[46] and more simply using a phase grating and an amplitude grating.[47,48] Since the interferometers use paraxial rays, interference is much less influenced by vibration than in the case of the crystal interferometers.

Here, the X-ray Talbot interferometer[47] shown in Fig. 8 is introduced. The Talbot interferometer is based on the Talbot effect,[49] or a self-imaging effect; under spatially coherent illumination of unit amplitude, the wave field $E(x, y, z)$ behind a transmission grating of a complex transmission function $T(x, y)$ at a specific distance $z = z_\text{T}$ is the same as $T(x, y)$. The effect is understood to be a result of the interference between diffraction orders from the grating or Fresnel diffraction. Denoting the period of the grating with d, $z_\text{T} = md^2/\lambda$, where m is an even integer. If m is an odd integer, a similar image corresponding to $T(x + d/2, y)$ is generated. Here, $T(x, y)$ is assumed to be modulated in the x direction. In the case of a phase grating ($T(x, y) = \exp[i\phi(x, y)]$), when m is a half integer,

$$|E(x, y, z_\text{T})|^2 = 1 + \sin[\phi(x, y) - \phi(x + d/2, y)], \quad (16)$$

which suggests that the visibility reaches 100% if $\phi(x, y)$ is modulated from 0 to $\pi/2$.

When an X-ray beam with a deformed wavefront passes through the grating, $E(x, y, z)$ is also deformed correspondingly. If a high-resolution image detector is employed to
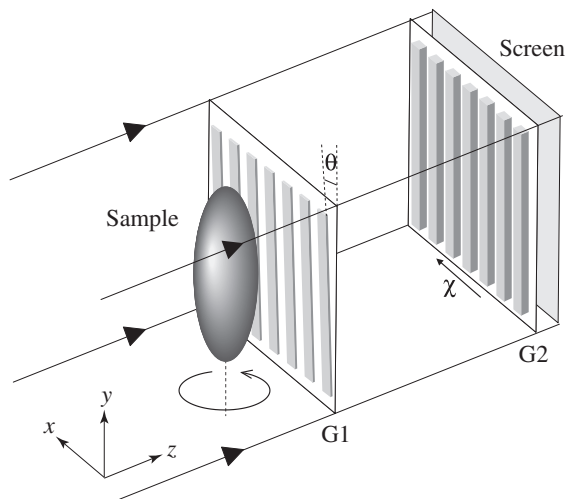
Fig. 8. X-ray Talbot interferometers used for phase imaging. A phase grating (G1) and an amplitude grating (G2) are aligned in line with a specific spacing determined by the period of the gratings and X-ray wavelength.

resolve the periodic pattern in $|E(x, y, z_T)|^2$, one can observe the deformation. Instead, an amplitude grating of a period d is placed at the position $z = z_T$ in an X-ray Talbot interferometer; the deformation is then visualized as a moiré pattern. Assuming a phase object in front of the first grating, the generated moiré pattern is given under the paraxial approximation by

$$I(x, y, z_T)$$
$$= \sum_n b_n(z_T)c_n \exp\left[i2\pi\frac{n}{d}\{y\theta + z_T\alpha_x(x, y) + \chi\}\right], \quad (17)$$

where $b_n(z_T)$ and c_n are the nth Fourier coefficients of $|E(x, y, z_T)|^2$ and the intensity transmission function of the second grating, respectively, and $\alpha_x(x, y)$ is given by eq. (12). Here, the gratings are slightly inclined by θ ($\ll 1$) in the x-y plane and displaced by χ in the y direction from each other. The spacing of moiré fringes d/θ is much larger than d, and is easily observed without a high-resolution image detector.

A difficulty in constructing an X-ray Talbot interferometer is the fabrication of the second grating, which must be an amplitude grating in principle to generate a contrast. Since d should be smaller than the spatial coherence length, a grating pattern with a high aspect ratio must be fabricated. Optical lithography would be unavailable for this purpose, and the X-ray LIGA (Lithographie, Galvanoformung, Abformung) process[50] is expected as an alternative approach to the fabrication of such a grating.[51]

Otherwise, a crystal is needed to select only the beams that suffered $+n$th diffraction at the first grating and $-n$th diffraction at the second grating, which is a phase grating, sequentially and $-n$th at the first and $+n$th at the second.[46] In this case, however, the throughput of the interferometer decreases sharply because of the crystal optics, while the X-ray Talbot interferometer functions for a spherical X-ray wave and its energy band width $\Delta E/E$ can be broadened up to $1/10$.[51] The medical application of the X-ray Talbot interferometer is therefore attractive.

For phase tomography, $\Phi(x, y)$ is determined by integrating $\alpha_x(x, y)$, which can be measured by changing the displacement χ in eq. (17) by a constant step, as in the fringe-scanning method. It should be noted, however, that eq. (15) is given for two beam interferometry, which generates sinusoidal fringe profiles. In the case of Talbot interferometry, multibeam interference occurs and higher orders may cause a systematic error. Nevertheless, using moiré patterns $I_k(x, y, z_T)$ obtained when $\chi = kd/M$ ($k = 1, 2, \ldots, M$),

$$y\theta + z_T\alpha_x(x, y)$$
$$\approx \frac{d}{2\pi}\arg\left[\sum_{k=1}^M I_k(x, y, z_T)\exp\left(-2\pi i\frac{k}{M}\right)\right] \quad (18)$$

can be used without crucial error because the partial coherence of X-rays decreases the influence of higher orders, and because the errors derived from specific orders satisfying $|n| = |qM + 1|$ (q: integer) are cancelled out mathematically.[52,53]

Figure 9 shows images of an ant obtained with 12.4 keV undulator X-rays using an X-ray Talbot interferometer consisting of two gold transmission gratings with an 8 μm period. The height of the gold pattern of the amplitude grating (G2) was 8 μm. Figure 9(b) was obtained using eq. (18) from moiré patterns, one of which is shown in Fig. 9(a), and a reconstructed tomogram is shown in Fig. 9(c).
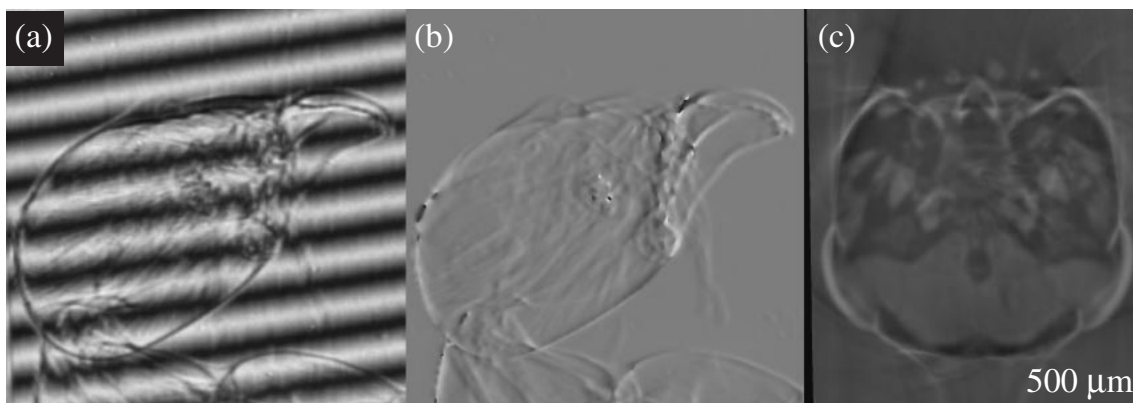

Fig. 9. Images of an ant obtained with 12.4 keV undulator X-rays by using X-ray Talbot interferometer: (a) moiré pattern, (b) differential phase, and (c) phase tomogram.
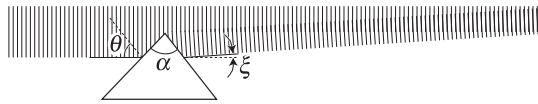
Fig. 10.   Interference caused by an X-ray prism.

4.2.3   Prism interferometer

Recently hard X-ray interferometric optics using a prism[62] has been studied (Fig. 10). As mentioned, the ratio δ/β is about 1000 for materials comparatively transparent to hard X-rays. Such materials can be used as an X-ray prism. For instance, δ and β of acrylic resin are 1.7×10^{-6} and 1.6×10^{-9} at 12.4 keV, respectively. The deflection angle ξ by a prism of an apex angle α is given by

$$\xi = \frac{\delta \sin \alpha}{\cos(\theta - \alpha) \cos \theta}, \tag{19}$$

where θ is the incident angle to the prism. Thus, ξ is of the order of 10^{-5}–10^{-6} rad in the case of an acrylic prism, and the beam can be shifted by 100–10 μm at 10 m downstream of the prism without crucial intensity loss. It should be noted that the beam deflection is opposite to that in the visible-light region because the refractive index is below unity in the X-ray region. Therefore, the deflected beam overlaps with the beam that goes past the prism. An interference field is generated there, producing fringes of a spacing λ/ξ, provided that the spatial coherence length is larger than ξ. Besides simple two-beam interferometry,[62] shearing interferometry[63] and holography[23] have also been attempted with a prism.

4.2.4   Soft X-ray interferometers

As mentioned, soft X-ray interferometry has progressed less than hard X-ray interferometers in spite of the longer wavelengths of soft X-rays. However, some interferometers using soft X-ray lasers are studied, taking advantage of its short pulse width and high peak brilliance, enabling instant acquisition of interference images. Pictures of interference fringes generated by Mach–Zehnder types using self-standing multilayers[54] or gratings[55,56] for splitting and recombining beams and by a Michelson type using self-standing multilayers[57] were able to be taken, although the optical elements were probably vibrating. The diagnosis of source plasma was a main target of the interferometers.

When synchrotron radiation is used, a longer exposure is normally required to take clear interference images, and therefore higher stability is required for the interferometer. Interferometers using a Fresnel mirror are comparatively easy to construct, and some imaging results have been reported so far.[58,59]

Interferometric microscopes using the focusing optics shown in Fig. 11, which were operated with synchrotron radiation, are introduced here. One is a phase-shifting point-diffraction interferometer and the other is a Mirau interferometer.

The phase-shifting point-diffraction interferometer reported by Naulleau et al.[60] consists of a transmission grating, a focusing test optic, which is to be evaluated with this system, and a mask. Two diffraction orders from the grating through the test optic make two spots at the mask. One spot can pass
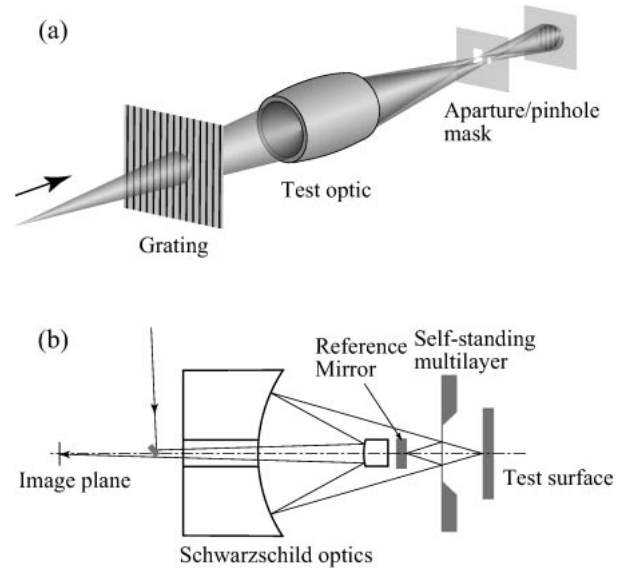

Fig. 11.   Soft X-ray interferometric microscopes: (a) phase-shifting point-diffraction interferometer[60] and (b) Mirau interferometer.[61]

through the mask and the other is used to make a reference beam through a pinhole made on the mask. The test optic is evaluated by resultant interference fringes, which are bent if the test optic is imperfect. This interferometer uses paraxial rays, and therefore is comparatively easy to operate.

The successful operation of a Mirau interferometer by Haga et al. is noteworthy.[61] They used a self-standing Mo/Si multilayer in combination with Schwarzschild optics with 13 nm synchrotron soft X-rays, and inspected defects 5 nm in height on an extreme ultraviolet lithography mask.

4.3   Refraction-based technique

Refraction is always accompanied by the spatially variant phase shift since waves propagate in the direction perpendicular to the wavefront. Therefore, a contrast related to the phase-shift gradient is generated by selecting refracted X-rays by a specific amount. As suggested by eq. (19), however, the deflection angle caused by refraction is extremely small, and X-rays are assumed conventionally to go straight through materials.

In order to generate the contrast, an angular sensor sufficiently sensitive to the X-ray refraction is needed and the incident X-rays should furthermore be correspondingly collimated. A candidate device for this purpose is a perfect crystal, in which X-rays are dynamically diffracted.[64–68] The angular width of the Bragg diffraction is of the order of 10^{-5} rad, which can easily be further narrowed down to 10^{-6} rad by using higher-order diffraction, asymmetrical diffraction and/or a multicrystal arrangement.

Figure 12 is a typical arrangement for generating a contrast based on the X-ray refraction using perfect crystals. When an X-ray beam collimated by a crystal passes through a sample, the wavefront is deformed by the phase shift at the sample and the X-ray propagation direction varies depending on the phase gradient. The analyzer crystal placed downstream of the sample reflects only the X-rays that meet the Bragg diffraction condition. As a result, a contrast can be seen in the reflected beam. By changing the angular setting of the analyzer slightly, the contrast varies sensitively.
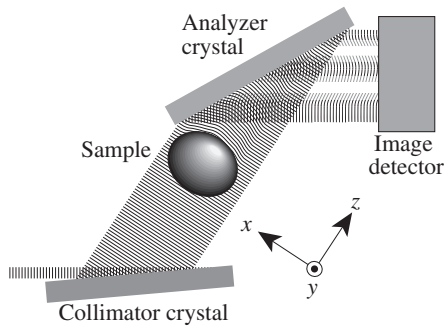
Fig. 12.   Typical setup for selecting refracted X-rays.

Medical applications of this technique are studied mainly for the diagnoses of breast and articular cartilage.[69–73]

Given the reflection curve $R(\theta)$ of the analyzer and the complex transmission function $\sqrt{A(x,y)}\exp[-i\Phi(x,y)]$ of the sample, the image $I(x, y, \theta_0)$ of the beam reflected by the analyzer is given by

$$I(x, y, \theta_0) = A(x,y)R(\theta_0 - \alpha_x(x,y)), \qquad (20)$$

where θ_0 is the incident angle without the sample. For phase tomography, $\Phi(x, y)$ is determined by integrating $\alpha_x(x, y)$, which can be measured with

$$\alpha_x(x,y) = \frac{\sum_k \theta_k I(x, y, \theta_k)}{\sum_k I(x, y, \theta_k)} \qquad (21)$$

by scanning the analyzer. The constant of integration in calculating $\Phi(x, y)$ is determined with the assumption, which is inherently required for tomographic measurement, that a sample is surrounded by a null region. The phase unwrapping procedure is not needed here. This measurement is repeated while rotating a sample on the axis parallel to the y direction shown in Fig. 12.

Figure 13 shows a demonstration of phase tomography with this technique using 20.7 keV X-rays. Figure 13(a) is a representative image obtained for an ant, setting the analyzer near the Bragg diffraction condition. $\alpha_x(x, y)$ calculated with eq. (21) is shown in Fig. 13(b). This measurement was repeated while rotating the sample with a 0.72° step, and the three-dimensional image shown in Fig. 13(c) was reconstructed.[74]

Another type of phase tomography was performed by rotating the sample on the axis parallel to the x direction.[75,76] In this case, $\alpha_x(x, y)$ can be dealt with as a scalar value, and therefore $\partial\delta/\partial x$ was reconstructed by processing $\alpha_x(x, y)$ directly.

4.4   Propagation-based technique

Conventionally, the distance between an object and an X-ray image detection plane should be as short as possible in order to avoid blurring. However, under spatially coherent illumination, Fresnel or Fraunhofer diffraction is observed at a distance away from an object even in the hard X-ray region.[77–81] Then, an edge-enhanced contrast is observed without optical elements even for a phase object, as illustrated in Fig. 14. Therefore, in this case setting a proper distance between an object and an X-ray image detection plane is essential.

In the X-ray region, a wave field propagating in the z direction is expressed under the paraxial approximation with

$$\frac{2\pi}{\lambda}\frac{\partial}{\partial z}I(x, y, z) = \nabla_\perp \cdot [I(x, y, z)\nabla_\perp\Phi(x, y, z)], \qquad (22)$$

which is known as the transport of intensity equation (TIE),[82] where $\nabla_\perp$ is the two-dimensional gradient operator acting in the x–y plane. Whereas the phase shift $\Phi(x, y)$ caused by a sample is assumed to be invariable along the optical axis in the methods described in §4.2 and §4.3, TIE can deal with the change of the wavefront brought about by propagation as $\Phi(x, y, z)$ in eq. (22).

Assuming weak absorption and unit-amplitude plane-wave illumination, eq. (22) is simplified as[83]

$$I(x, y, z) \approx 1 + \frac{\lambda z}{2\pi}\nabla_\perp^2\Phi(x, y, 0), \qquad (23)$$

Fig. 14.   Illustration showing the generation of an edge enhanced contrast of a phase object due to propagation.
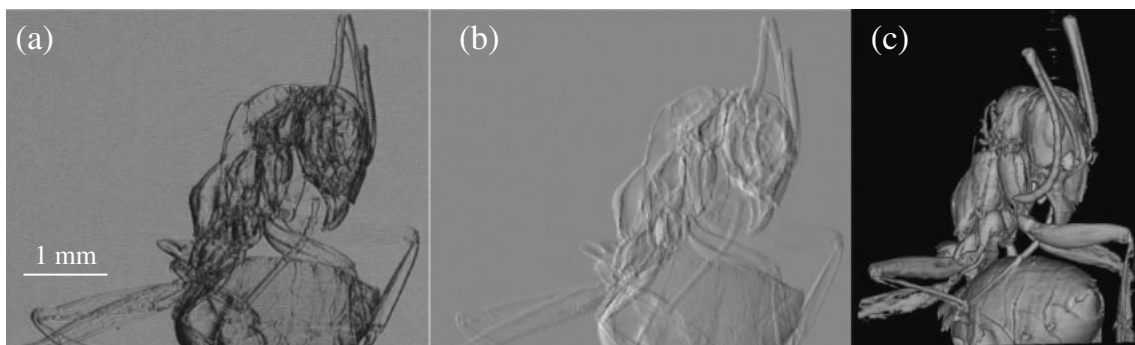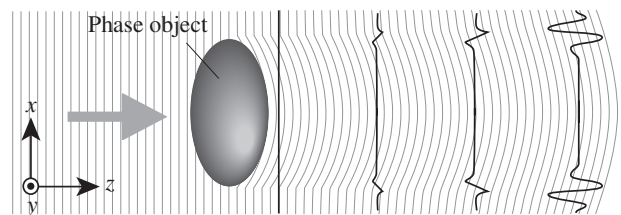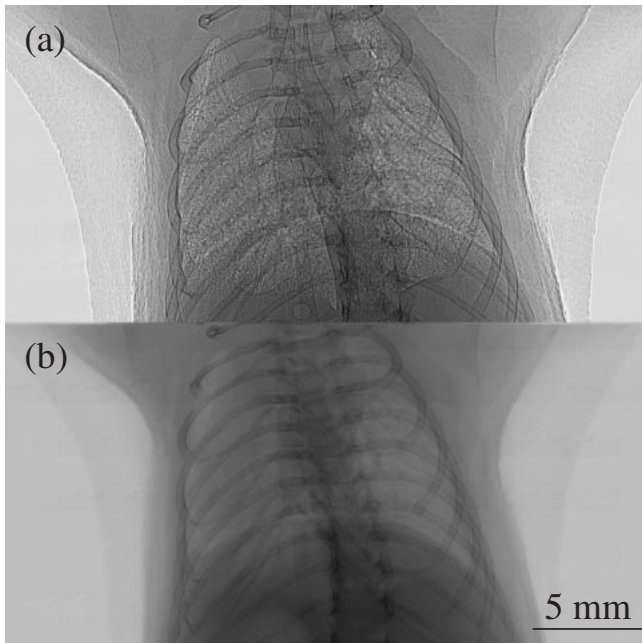

Fig. 13.   Ant observed by extracting refracted 20.7 keV X-rays with an analyzer crystal. (a) Image observed by setting the analyzer near the Bragg diffraction condition. (b) Image mapping the angle of beam deflection calculated from images obtained by scanning the analyzer around the Bragg diffraction angle. (c) Three-dimensional image reconstructed by phase tomography.[74]

Fig. 15.   Images of the thorax of a nude mouse obtained with 28.8 keV undulator X-rays.[84] Edge enhancement is prominent in the image (a) obtained 6.5 m downstream of the mouse in comparison with the contact image (b).
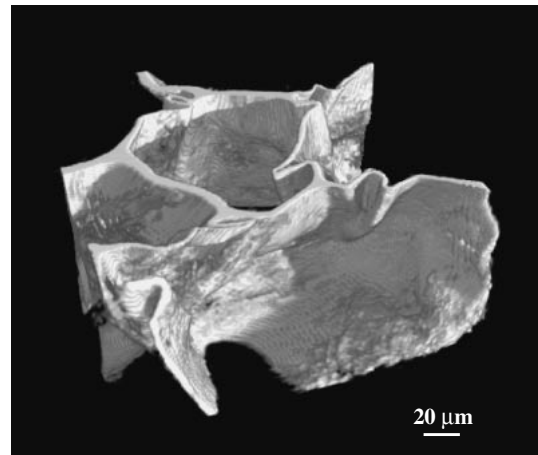

Fig. 16.   Image of a polystyrene foam obtained with 18 keV undulator X-rays by using phase tomography based on the contrast caused by wave propagation.[92]

which suggests the generation of the contrast outlining surfaces and structural boundaries, where the refractive index changes abruptly. As demonstrated in Fig. 15(a), which shows a transmission image of the thorax of a nude mouse[84] measured 6.5 m downstream with 28.8 keV undulator X-rays, edge enhancement is clear in comparison with a contact image [Fig. 15(b)] which corresponds to an absorption image. Besides the third-generation synchrotron radiation sources, microfocus X-ray generators can be used to perform imaging with this phenomenon, and in addition to microscopic applications,[85–87] medical applications[88–91] have been attempted.

Phase tomography has been demonstrated in the microscopic studies of this technique.[92,93] $\Phi(x, y)$ was determined from a near-field image based on TIE under the condition that the spatial resolution and the signal-to-noise ratio were sufficient.[94] By observing intermediate-field images at various z positions where the Fresnel number was around unity, $\Phi(x, y)$ was also determined,[92] using a recursive procedure.[95] The phase unwrapping procedure was not needed in this case. Figure 16 shows an image of a polystyrene foam observed with 18 keV undulator X-rays.

5. Future Prospects

As described, it seems that the field of X-ray phase imaging aims at two targets. One is to innovate X-ray microscopy, particularly improving spatial resolution, and the other is to innovate on radiography, improving the sensitivity and correspondingly reducing the X-ray dose.

The development of optical elements, such as the Fresnel zone plate, focusing mirror, and compound refractive lens, has continued to improve the spatial resolution of X-ray microscopy. The high sensitivity of phase imaging of course contributes to a better spatial resolution. It should be emphasized that the phase imaging is significant for

revealing structures below the size of one micron. The quality of the optical elements is determined in short by their ability to control the X-ray phase, and the development of high-quality optical elements enables the generation of clear phase-contrast. For future X-ray microscopy, controlling and measuring the X-ray phase is indispensable.

Of course, the advance in X-ray sources plays an important role as well, and it is not too much to say that third-generation synchrotron radiation sources promoted the activity of X-ray phase imaging. Furthermore, the next-generation X-ray sources such as the X-ray free-electron laser currently under construction[96–98] are opening up new possibilities toward molecular imaging, as mentioned in §4.1.4. Although its technique is in an early stage of development, its potential to go far beyond conventional imaging techniques attracts attention from many researchers.

Introducing the techniques of X-ray phase imaging into radiography, particularly those with a wide field of view, would be important from a medical point of view. Medical applications are mentioned in many studies of X-ray phase imaging. Therefore, although high spatial resolution is welcome provided that the required X-ray dose is permissible, the field of view is a more important aspect than the spatial resolution.

Two courses for medical application are considered: one involves using synchrotron radiation and the other using a compact X-ray source. Because coherence is needed to some extent for phase imaging, the use of a bright X-ray source is preferable to compensate for the loss of X-ray intensity by coherence filtering. Particularly when crystal optics is used, synchrotron radiation would be indispensable. Furthermore, because synchrotron radiation, especially undulator radiation, is normally a thin beam, a device for beam expansion such as the collimator crystal shown in Fig. 12 is necessary.

If regular medical applications of X-ray phase imaging are expected to benefit from the attractive image obtained by using synchrotron radiation, synchrotron radiation facilities dedicated for medical applications should be constructed. However, the combination of a compact X-ray source with the X-ray phase imaging techniques would be preferable from a practical point of view even if the image quality is degraded to some extent compared with that obtained by

synchrotron radiation. A spherical X-ray wave from a compact X-ray source is a great advantage in creating a field of view as wide as is required. Unfortunately, however, conventional X-ray sources are not available because of their poor spatial coherency. The key therefore is the development of a microfocus X-ray generator specialized for phase imaging. In addition, because of the limited X-ray flux available from the source, an apparatus should be developed employing optical elements that function with a broad bandwidth, such as the gratings described in §4.2.2, or without an optical element, as described in §4.4.

6. Summary

In this article, X-ray phase imaging germinated in the past decade was reviewed. Since the interaction cross section of the X-ray phase shift is about a thousand times larger than that of absorption, an extremely high sensitivity is attained by X-ray phase imaging, enabling the observation of biological soft tissues and organic materials. The phase shift accompanies refraction, and various imaging methods are studied using interference phenomena and/or by selecting refracted X-rays. In X-ray microscopy, making it possible to measure and control the X-ray phase will become more important, and ultimately the spatial resolution is approaching molecular sizes. Besides microscopic application, X-ray phase imaging is attractive for medical diagnosis and nondestructive investigation. For practical applications, a breakthrough in incorporating the techniques of X-ray phase imaging into apparatuses outside synchrotron facilities would be necessary, and some approaches have already been attempted.

Novel phase imaging methods have still been proposed and attempted so vigorously that the current activities may not be covered fully in this article. The past decade was the beginning of a great innovation in X-ray imaging from the viewpoint of the history of X-rays. Although many problems remain unsolved, further developments in X-ray sources and optical elements are expected to be steady, and the future of X-ray phase imaging is promising with fruitful applications sure to come.

1) J. Als-Nielsen and D. McMorrow: *Elements of Modern X-Ray Physics* (John Wiley & Sons, Chichester, 2001) p. 21.
2) R. Fitzgerald: Phys. Today (June, 2000) 23.
3) A. Momose and J. Fukuda: Med. Phys. **22** (1995) 375.
4) A. Momose: Nucl. Instrum. Methods Phys. Res., Sect. A **352** (1995) 622.
5) Monochromatization of soft X-rays neighboring the hard X-ray region ($\lambda \approx 1$ nm) is comparatively difficult. Activity of phase imaging is comparatively low in this region.
6) M. Born and E. Wolf: *Principle of Optics* (Pergamon Press, Oxford, 1980) p. 508.
7) *Handbook of Optics: Classical Optics, Vision Optics, X-Ray Optics*, eds. M. Bass *et al.* (McGraw-Hill, New York, 2001) Part 3.
8) A. Snigirev, V. Kohn, I. Snigireva and B. Lengeler: Nature **384** (1996) 49.
9) J. Kirz, C. Jacobsen and M. Howells: Q. Rev. Biol. **28** (1995) 33.
10) A. Authier: *Dynamical Theory of X-Ray Diffraction* (Oxford Univ. Press, Oxford, 2001).
11) M. Awaji, Y. Suzuki, A. Takeuchi, H. Takano, N. Kamijo, S. Tamura and M. Yasumoto: J. Synchrotron Radiat. **9** (2002) 125.
12) F. Zernike: Z. Tech. Phys. **16** (1935) 454.
13) G. Schmahl, D. Rudolph, P. Guttmann, G. Schneider, J. Thieme, B. Niemann and T. Wilhein: Synchrotron Radiat. News **7** (1994) No. 4, 19.
14) Y. Kagoshima, T. Ibuki, Y. Yokoyama, Y. Tsusaka, J. Matsui, K. Takai and M. Aino: Jpn. J. Appl. Phys. **40** (2001) L1190.
15) U. Newhäusler, G. Schneider, W. Ludwig, M. A. Meyer, E. Zschech and D. Hambach: J. Phys. D **36** (2003) A79.
16) D. Gabor: Nature **161** (1948) 777.
17) S. Kikuta, S. Aoki, S. Kosaki and K. Kohra: Opt. Commun. **5** (1972) 86.
18) S. Aoki and S. Kikuta: Jpn. J. Appl. Phys. **13** (1974) 1385.
19) I. McNulty, J. Kirz, C. Jacobsen, E. H. Anderson, M. R. Howells and D. P. Kern: Science **256** (1992) 1009.
20) S. Eisebitt, J. Lüning, W. F. Schlotter, M. Lürgen, O. Hellwig, W. Eberhardt and J. Stöhr: Nature **432** (2004) 885.
21) W. Leitenberger and A. Snigirev: J. Appl. Phys. **90** (2001) 538.
22) N. Watanabe, H. Kokosuka, T. Ohigashi, H. Takano, A. Takeuchi, Y. Suzuki and S. Aoki: J. Phys. IV (Paris) **104** (2003) 551.
23) Y. Kohmura, T. Sakurai, T. Ishikawa and Y. Suzuki: J. Appl. Phys. **96** (2004) 1781.
24) T. Wilhein, B. Kaulich, E. Di Fabrizio, F. Romanato, S. Cabrini and J. Susini: Appl. Phys. Lett. **78** (2001) 2082.
25) H. N. Chapman, C. Jacobsen and S. Williams: Rev. Sci. Instrum. **66** (1995) 1332.
26) H. Takano, K. Uesugi, A. Takeuchi, K. Takai and Y. Suzuki: J. Phys. IV (Paris) **104** (2003) 41.
27) Y. Kagoshima, K. Shimose, T. Koyama, I. Wada, A. Saikubo, K. Hayashi, Y. Tsusaka and J. Matsui: Jpn. J. Appl. Phys. **43** (2004) L1449.
28) J. Miao, P. Charalambous, J. Kirz and D. Sayre: Nature **400** (1999) 342.
29) J. Miao, T. Ishikawa, B. Johnson, E. H. Anderson, B. Lai and K. O. Hodgson: Phys. Rev. Lett. **89** (2002) 088303.
30) A. Momose: J. Synchrotron Radiat. **9** (2002) 136.
31) A. Momose: Opt. Express **11** (2003) 2303.
32) U. Bonse and M. Hart: Appl. Phys. Lett. **6** (1965) 155.
33) M. Ando and S. Hosoya: Proc. 6th Int. Conf. X-ray Optics and Microanalysis, Univ. Tokyo, 1972, p. 63.
34) A. Momose, T. Takeda, Y. Itai and K. Hirano: Nat. Med. **2** (1996) 473.
35) F. Beckmann, U. Bonse, F. Busch and O. Günnewig: J. Comput. Assist. Tomogr. **21** (1997) 539.
36) T. Takeda, A. Momose, E. Ueno and Y. Itai: J. Synchrotron Radiat. **5** (1998) 1133.
37) T. Takeda, A. Momose, K. Hirano, S. Haraoka, T. Watanabe and Y. Itai: Radiology **214** (2000) 298.
38) A. Momose, I. Koyama, Y. Hamaishi, H. Yoshikawa, T. Takeda, J. Wu, Y. Itai, K. Takai, K. Uesugi and Y. Suzuki: J. Phys. IV (Paris) **104** (2003) 599.
39) M. Takeda, H. Ina and S. Kobayashi: J. Opt. Soc. Am. **72** (1982) 156.
40) J. H. Bruning, D. R. Herriott, J. E. Gallagher, D. P. Rosenfeld, A. D. White and D. J. Brangaccio: Appl. Opt. **13** (1974) 2693.
41) J. M. Huntley: Appl. Opt. **28** (1989) 3268.
42) A. Yoneyama, T. Takeda, Y. Tsuchiya, J. Wu, Thet Thet Lwin, A. Koizumi, K. Hyodo and Y. Itai: Nucl. Instrum. Methods Phys. Res., Sect. A **523** (2004) 217.
43) T. Takeda, A. Yoneyama, J. Wu, Thet Thet Lwin, Y. Tsuchiya and K. Hyodo: Jpn. J. Appl. Phys. **43** (2004) L1144.
44) K. Iwata, H. Kikuta, H. Tadano, H. Hagino and T. Nakano: Jpn. J. Appl. Phys. **38** (1999) 6535.
45) I. Koyama, H. Yoshikawa and A. Momose: Jpn. J. Appl. Phys. **42** (2003) L80.
46) C. David, B. Nöhammer, H. H. Solak and E. Ziegler: Appl. Phys. Lett. **81** (2002) 3287.
47) A. Momose, S. Kawamoto, I. Koyama, Y. Hamaishi, K. Takai and Y. Suzuki: Jpn. J. Appl. Phys. **42** (2003) L866.
48) T. Weitkamp, B. Nöhammer, A. Diaz and C. David: Appl. Phys. Lett. **86** (2005) 054101.
49) H. F. Talbot: Philos. Mag. **9** (1836) 401.
50) E. W. Becker, W. Ehrfeld, P. Hagmann, A. Maner and D. Munchmeyer: Microelectron. Eng. **4** (1986) 35.
51) A. Momose, S. Kawamoto, I. Koyama and Y. Suzuki: Proc. SPIE **5535** (2004) 352.
52) K. A. Stetson and W. R. Brohinsky: Appl. Opt. **24** (1985) 3631.
53) T. Pfeifer, B. Wang, J. Evertz and R. Tutsch: Optik **98** (1995) 158.

54) L. B. Da Silva, T. W. Barbee, Jr., R. Cauble, P. Celliers, D. Ciarlo, S. Libby, R. A. London, D. Matthews, S. Mrowka, J. C. Moreno, D. Ress, J. E. Trebes, A. S. Wan and F. Weber: Phys. Rev. Lett. **74** (1995) 3991.

55) J. Filevich, K. Kanizay, M. C. Morconi, J. L. A. Chilla and J. J. Rocca: Opt. Lett. **25** (2000) 356.

56) J. Filevich, J. J. Rocca, M. C. Marconi, R. F. Smith, J. Dunn, R. Keenan, J. R. Hunter, S. J. Moon, J. Nilsen, A. Ng and V. N. Shlyaptsev: Appl. Opt. **43** (2004) 3938.

57) F. Delmotte, M.-F. Ravet, F. Bridou, F. Varniere, P. Zeitoun, S. Hubert, L. Vanbostal and G. Soullie: Appl. Opt. **41** (2002) 5905.

58) D. Joyeux and F. Polack: in *X-Ray Microscopy and Spectromicroscopy*, eds. J. Thieme, G. Schmahl, D. Rudolph and E. Umbach (Springer, Berlin, 1998) p. II.103.

59) D. Joyeux, R. Mercier, D. Phalippou, M. Mullot, S. Hubert, P. Zeitoun, A. Carillon, A. Klisnick, G. Jamelot, E. Bechir and G. de Lacheze-Murel: AIP Conf. Proc. **507** (2000) 511.

60) P. P. Naulleau, K. A. Goldberg, S. H. Lee, C. Chang, D. Attwood and J. Bokor: Appl. Opt. **38** (1999) 7252.

61) T. Haga, H. Takenaka and M. Fukuda: J. Vac. Sci. Technol. B **18** (2000) 2916.

62) Y. Suzuki: Jpn. J. Appl. Phys. **41** (2002) L1019.

63) Y. Kohmura, T. Ishikawa, H. Tadano, H. Hagino and Y. Suzuki: J. Appl. Phys. **93** (2003) 2283.

64) V. A. Somenkov, A. K. Tkalich and S. Sh. Shil'shtein: Sov. Phys. Tech. Phys. **36** (1991) 1309.

65) T. J. Davis, D. Gao, T. E. Gureyev, A. W. Stevenson and S. W. Wilkins: Nature **373** (1995) 595.

66) V. N. Ingal and E. A. Beliaevskaya: J. Phys. D **28** (1995) 2314.

67) D. Chapman, W. Thomlinson, R. E. Johnston, D. Washburn, E. Pisano, N. Gmür, Z. Zhong, R. Menk, F. Arfelli and D. Sayers: Phys. Med. Biol. **42** (1997) 2015.

68) M. Ando, H. Sugiyama, A. Maksimenko, W. Pattanasiriwisawa, K. Hyodo and X. Zhang: Jpn. J. Appl. Phys. **40** (2001) L844.

69) V. N. Ingal, E. A. Beliaevskaya, A. P. Brianskaya and R. D. Merkurieva: Phys. Med. Biol. **43** (1998) 2555.

70) E. D. Pisano, R. E. Johnston, D. Chapman, J. Geradts, M. V. Iacocca, C. A. Livasy, D. B. Washburn, D. E. Sayers, Z. Zhong, M. Z. Kiss and W. C. Thomlinson: Radiology **214** (2000) 895.

71) R. A. Lewis, C. J. Hall, A. P. Hufton, S. Evans, R. H. Menk, F. Arfelli, L. Rigon, G. Tromba, D. R. Dance, I. O. Ellis, A. Evans, E. Jacobs, S. E. Pinder and K. D. Rogers: Br. J. Radiol. **76** (2003) 301.

72) S. Majumdar, A. S. Issever, J. Lotz, F. Arfelli, L. Rigon, G. Heitner and R. H. Menk: Eur. Radiol. **14** (2004) 1440.

73) M. Ando, H. Sugiyama, T. Kunisada, D. Shimao, K. Takeda, H. Hashizume and H. Inoue: Jpn. J. Appl. Phys. **43** (2004) L1175.

74) I. Koyama, Y. Hamaishi and A. Momose: AIP Conf. Proc. **705** (2004) 1283.

75) F. A. Dilmanian, Z. Zhong, B. Ren, X. Y. Wu, L. D. Chapman, I. Orion and W. C. Thomlinson: Phys. Med. Biol. **45** (2000) 933.

76) S. Fiedler, A. Bravin, J. Keyriläinen, M. Fernández, P. Suortti, W. Thomlinson, M. Tenhunen, P. Virkkunen and M.-L. Karjalainen-Lindsberg: Phys. Med. Biol. **49** (2004) 175.

77) A. Snigirev, I. Snigireva, V. Kohn, S. Kuznetsov and I. Schelokov: Rev. Sci. Instrum. **66** (1995) 5486.

78) K. A. Nugent, T. E. Gureyev, D. F. Cookson, D. Paganin and Z. Barnea: Phys. Rev. Lett. **77** (1996) 2961.

79) P. Cloetens, R. Barret, J. Baruchel, J. P. Guigay and M. Schlenker: J. Phys. D **29** (1996) 133.

80) S. W. Wilkins, T. E. Gureyev, D. Gao, A. Pogany and A. W. Stevenson: Nature **384** (1996) 335.

81) Z. H. Hu, P. A. Thomas, A. Snigirev, I. Snigireva, A. Souvorov, P. G. R. Smith, G. W. Ross and S. Teat: Nature **392** (1998) 690.

82) M. R. Teague: J. Opt. Soc. Am. **73** (1983) 1434.

83) J. M. Cowley: *Diffraction Physics* (Elsevier, Amsterdam, 1995) Chap. 3.

84) N. Yagi, Y. Suzuki, K. Umetani, Y. Kohmura and K. Yamasaki: Med. Phys. **26** (1997) 2190.

85) S. Di Fonzo, W. Jark, S. Lagomarsino, C. Giannini, L. De Caro, A. Cedola and M. Müller: Nature **403** (2000) 638.

86) B. E. Allman, P. J. McMahon, J. B. Tiller, K. A. Nugent, D. Paganin and A. Barty: J. Opt. Soc. Am. A **17** (2000) 1732.

87) S. C. Mayo, T. J. Davis, T. E. Gureyev, P. R. Miller, D. Paganin, A. Pogany, A. W. Stevenson and S. W. Wilkins: Opt. Express **11** (2002) 2289.

88) C. J. Kotre and I. P. Birch: Phys. Med. Biol. **44** (1999) 2853.

89) F. Arfelli, V. Bonvicini, A. Bravin, G. Cantatore, E. Castelli, L. Dalla Palma, M. Di Michiel, M. Fabrizioli, R. Longo, R. H. Menk, A. Olivo, S. Pani, D. Pontoni, P. Poropat, M. Prest, A. Rashevsky, M. Ratti, L. Rigon, G. Tromba, A. Vacchi, E. Vallazza and F. Zanconati: Radiology **215** (2000) 286.

90) A. Ishisaka, H. Ohara and C. Honda: Opt. Rev. **7** (2000) 566.

91) K. Mori, N. Sekine, H. Sato, N. Shikano, D. Shimao, H. Shiwaku, K. Hyodo and K. Ohashi: Jpn. J. Appl. Phys. **41** (2002) 5490.

92) P. Cloetens, W. Ludwig, J. Baruchel, D. Van Dyck, J. Van Landuyt, J. P. Guigay and M. Schlenker: Appl. Phys. Lett. **75** (1999) 2912.

93) P. J. McMahon, A. G. Peele, D. Paterson, J. J. A. Lin, T. H. K. Irving, I. McNulty and K. A. Nugent: Opt. Commun. **217** (2003) 53.

94) T. E. Gureyev, C. Raven, A. Snigirev, I. Snigireva and S. W. Wilkins: J. Phys. D **32** (1999) 563.

95) W. Coene, G. Janssen, M. Op de Beeck and D. Van Dyck: Phys. Rev. Lett. **69** (1992) 3743.

96) *LCLS the First Experiments* (Stanford Linear Accelerator Center, Stanford, 2000); http://www-ssrl.slac.stanford.edu/lcls/

97) *TESLA Technical Design Report Part V: The X-ray Free Electron Laser* (Deutsches Elektronen Synchrotron, Hamburg, 2001); http://xfel.desy.de/content/xfelhomepage/index_eng.html/

98) T. Shintake, H. Kitamura and T. Ishikawa: AIP Conf. Proc. **705** (2004) 117; http://www-xfel.spring8.or.jp/

Atsushi Momose was born in Toyama Prefecture, Japan in 1962. He received M.S. degree in Applied Physics from the University of Tokyo in 1987. He joined Hitachi, Ltd., Advanced Research Laboratory in 1987. He earned his Doctor's degree in Engineering from the University of Tokyo in 1996. He worked as a visiting scientist at the European Synchrotron Radiation Facility, France from 1997 to 1998. He moved to School of Engineering, The University of Tokyo in 1999 and then to Graduate School of Frontier Sciences, The University of Tokyo in 2003 as an associated professor. He has been pioneering X-ray phase imaging using synchrotron radiation. From 1997 to 2002, he conducted a project of phase imaging for medical applications supported through Special Coordination Funds of the Science and Technology Agency of the Japanese Government. From 2004, he started a connecting project supported by SENTAN of Japan Science and Technology Agency. He awarded a best paper prize in 1996 from Japanese Association of Radiological Physicists, and a young scientist prize in 1997 from Japanese Society of Synchrotron Radiation. He is a member of SPIE, U.S.A., the Japan Society of Applied Physics, the Physical Society of Japan, Japanese Society of Synchrotron Radiation, and Japan Society of Medical Physics.